



Exploring Design Options for Wing Leading Edge Against Bird Strike

Muhammed Cihan Tezel*

TOBB University of Economics and Technology, 06560 Ankara, Turkey

Yusuf Yamaner† and Bilge Aziz Çoğuz‡

Turkish Aerospace Industries, Inc., 06980 Ankara, Turkey

and

Erdem Acar§

TOBB University of Economics and Technology, 06560 Ankara, Turkey

<https://doi.org/10.2514/1.C036753>

This study investigates the effects of bird strike on the wing leading edge of a trainer aircraft in accordance with the European Aviation Safety Agency's CS-23 standards ("Normal, Utility, Aerobatic and Commuter Aeroplanes," Certification Specifications, Part 23, Occupant Physical Environment), and it compares various options for the design of energy-absorbing support structures. In this study, the bird model with hemispherical-ended cylindrical geometry is simulated using the smoothed particle hydrodynamics finite element approach. After validating the impact of the bird model on a rigid plate, a bird strike on the wing leading edge is modeled; and the results are compared with the existing experimental and simulation data available in the literature. Finally, different design options for the support structure configurations of the wing leading edge (including traditional rib design, honeycomb sandwich, triangular reinforcement, and negative Poisson ratio structures) are evaluated, and the results are compared. It is found that a honeycomb sandwich panel support structure provides the best collision and weight performance.

Nomenclature

C_1, \dots, C_6	=	LS-DYNA's EOS_LINEAR_POLYNOMIAL card coefficients
E_{11}	=	elastic modulus E_{AAU} in uncompressed configuration
E_{22}	=	elastic modulus E_{BBU} in uncompressed configuration
E_{33}	=	elastic modulus E_{CCU} in uncompressed configuration
E_{comp}	=	Young's modulus for compacted honeycomb material
E_{unc}	=	Young's modulus for uncompactd honeycomb material
FD	=	dynamic friction coefficient
FS	=	static friction coefficient
G_{12}	=	shear modulus G_{ABU} in uncompressed configuration
G_{13}	=	shear modulus G_{ACU} in uncompressed configuration
G_{23}	=	shear modulus G_{ABU} in uncompressed configuration
h	=	cell's height and edge length
IHQ	=	hourglass viscosity type
QH	=	hourglass coefficient
$Q1$	=	quadratic viscosity coefficient
$Q2$	=	linear viscosity coefficient
t	=	thickness of the edge
θ	=	angle of the cell's edge to the vertical axis
l	=	cell's edge length

I. Introduction

COLLISIONS between aircraft and birds affect flight safety, resulting in financial losses and the possible loss of lives. Aviation authorities such as the Federal Aviation Administration (FAA) and the European Aviation Safety Agency (EASA) have published regulations to reduce the detrimental effects of accidents and ensure flight safety. According to crash reports and statistics, windshields, radomes, engines, wings, and empennages are parts that have been damaged by bird strikes [1]. The FAA has reported a total of 222,753 bird ingestion accidents during the period of 1990–2018 [2,3]. To ensure that aircraft structures are resistant to bird strikes, experimental tests are carried out on the aircraft structural parts most likely to be affected by an impact. The repetition of experimental testing, the reproduction of the leading-edge structure, and the development of designed parts are costly and time-consuming processes. Numerical simulations are therefore used to analyze bird strikes, owing to their low computational cost and high accuracy.

To examine the bird-strike problem in detail, the behavior of the bird at the time of impact should be considered. In the experimental studies by Barber et al. [4], the impact of a bird on a rigid plate was investigated, where the impact pressure on the bird was determined. With the development of computers and the decrease in calculation costs, simulation-based studies have been widely used to solve bird impact problems. Lavoie et al. [5] conducted an experiment that compared physically impinging a gelatin bird model on a plate to a crash model generated using the LS-DYNA software package, and they found that simulation-based studies can provide close results to those obtained through experiments. Shupikov et al. [6] offered a new bird dummy model for testing the bird-strike resistance of aircraft components. The proposed bird dummy model was made of silicon that models the bird's muscular tissue, and it had plastic ball fillers for modeling the skeleton and the cavities inside the bird; it differed from existing analogs by reproducing the impact impulse with high accuracy.

Light weight and high strength are important design criteria in aviation. Various support structures have been designed to reduce the effects of bird strikes at the leading edges of aircraft wings. Innovative designs such as sandwich panels and triangular reinforcement structures have been used along with newly developed materials and production technologies. Hanssen et al. [7] conducted experimental and numerical simulations involving bird strikes using foam-based

Received 23 November 2021; revision received 13 May 2022; accepted for publication 4 June 2022; published online 26 July 2022. Copyright © 2022 by Erdem Acar. Published by the American Institute of Aeronautics and Astronautics, Inc., with permission. All requests for copying and permission to reprint should be submitted to CCC at www.copyright.com; employ the eISSN 1533-3868 to initiate your request. See also AIAA Rights and Permissions www.aiaa.org/randp.

*Graduate Student, Department of Mechanical Engineering, Söğütözü.

†Structural Engineer, Kahramankazan.

‡Integrated Product Team Leader, Kahramankazan.

§Associate Professor, Department of Mechanical Engineering, Söğütözü. Associate Fellow AIAA.

aluminum sandwich panels. This model was used to determine the minimum foam thickness that can handle bird-strike effects. Guida et al. [8,9] conducted an experimental and numerical study aimed at assessing the bird-strike resistance of a fiber-metal-laminate-composite leading edge for the wing of a transport aircraft. Smojver and Ivančević [10] modeled impact behavior using sandwich panels formed by composite and Nomex honeycomb structures on wing edges. Zhang et al. [11] investigated the performance of a wing leading edge, including spars and ribs with several material models, against impact with a bird and a tree. Liu et al. [12] introduced triangular reinforcement elements as an innovative design, compared the triangular reinforcement elements produced using different design techniques, and confirmed the simulation results through experiments. Similarly, Liu et al. [13] compared honeycomb and foam support structures in terms of their crash performance, and they found that the honeycomb exhibited better crash performance. Di Caprio et al. [14] used a numerical model to examine collision-resistant leading edges having different core configurations and thicknesses in honeycomb structures. The results demonstrated that thicker honeycomb structures and thicker shells provided the highest reduction in deformation by absorbing the high energy generated during a bird strike. Arachchige et al. [15] analyzed the effects of the skin thickness, layups, and impact velocities of a sandwich composite leading edge. They found that a quasi-isotropic layup performed better in terms of damage tolerance when it was compared with a cross-ply layup for the honeycomb reinforcement.

Negative Poisson's ratio (NPR) structures have been used as energy-absorbing structures in various industries, including aircraft and automotive industries [16,17]. Wang et al. [16] considered a typical fuselage section of aircraft during a crash landing, and they found that the fuselage section with the NPR structure showed better energy absorption capacity than the one without the NPR structure. In this study, we propose the use of NPR structures as wing leading-edge support structures for the first time in the literature (to the best of our knowledge). Another contribution of this study is that a thorough comparison of the effectiveness of existing as well as novel design options for support structures of a wing leading edge is conducted, and the best design option in terms of both crash and weight performance is determined.

The remainder of this paper is organized as follows. Section II presents the models used in the analysis of the bird strike against the

wing leading edge of a trainer aircraft, and it provides an overview of these models. Section III presents the validation studies conducted for the bird model as well as for the leading-edge finite element (FE) model. The finite element modeling of various support structures of the wing leading edge is explained in Sec. IV, and the impact performances of these structures are compared in Sec. V to determine an optimal design option for providing the best crash performance and lightest weight. Finally, concluding remarks are presented in Sec. VI.

II. Solution Methodology

In this study, a bird strike on the wing leading edge of a trainer aircraft is analyzed using the finite element software LS-DYNA through the combined use of three models: 1) the bird model, 2) the wing leading-edge model, and 3) an energy-absorbent support structure model. The flowchart in Fig. 1 describes the simulation of a bird strike on the wing leading edge. The details of each model are presented in the following sections.

The bird model includes FE modeling, equation of state modeling, bird geometry construction, and determination of proper hourglass and viscosity parameters. As shown in Fig. 2, the soft body of the bird during a high-speed impact potentially allows the use of Lagrangian, arbitrary Lagrangian-Eulerian (ALE), Eulerian, or smoothed particle hydrodynamics (SPH) as methods that can be used to obtain the FE model solution [18]. In the Lagrangian model, the nodes are fixed to the material; whereas in the Eulerian model, the nodes stay fixed and the material flows through the mesh. In the ALE model, the Eulerian mesh moves and deforms with the material flowing inside; whereas in SPH model, the fluid is modeled with SPH particles that can freely move.

In various studies, Lagrange, ALE, and SPH methods were used in bird-strike problems; and these three methods have been compared in other studies, which have concluded that the Lagrange method does not provide reliable results at high deformations, the ALE method incurs high computational costs, and the SPH method is preferable because of its lower computational cost as compared to the ALE method. In addition, according to the experimental and simulation behaviors of the bird, the SPH method produces the closest results to experimental results [19,20]. Various studies in the literature have also indicated their preference for the SPH method [8,21].

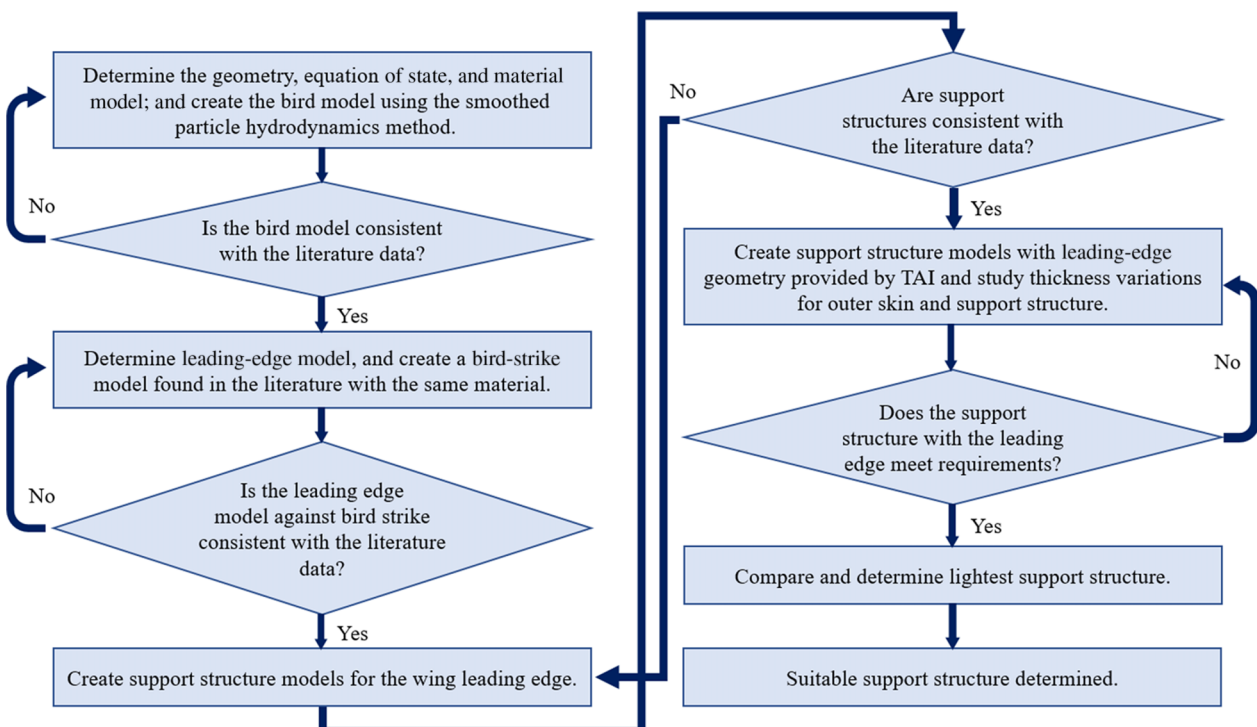


Fig. 1 Flowchart of the analysis of the wing leading edge against bird strike.

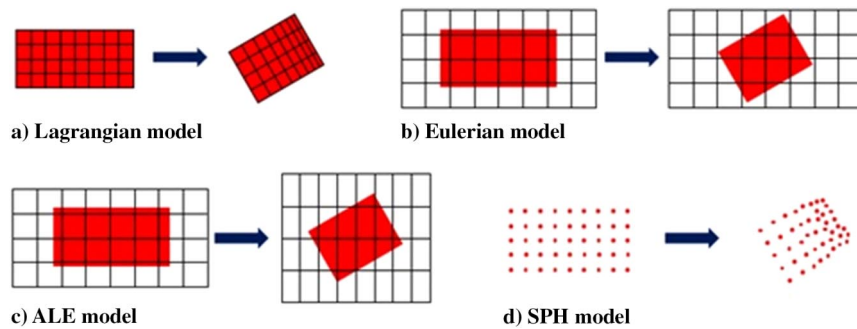


Fig. 2 Different FE approaches: a) Lagrangian, b) Eulerian, c) ALE, and d) SPH.

Cylinder, spherical, and hemispherical-ended spherical geometries are widely used in the literature to simplify the bird geometry. It was found that the hemispherical-ended cylinder bird model yields the closest impact behavior to that of a natural bird [22–24]. Consequently, the SPH method with a hemispherical-ended cylinder, as shown in Fig. 3, is used in this study.

Owing to the high-velocity impact, a bird's deformation is considered under four different categories: elastic, plastic, hydrodynamic, and explosive. As the internal stresses exceed the strength of the skin material, the hydrodynamic zone transition causes the skin to behave like a liquid [25]. Accordingly, birds are modeled using a mixture of water and air. To determine the hydrodynamic response of this fluid mixture, an equation of state (EOS) is required to accurately simulate the material's behavior. An EOS determines the hydrostatic behavior of a material by calculating the pressure as a function of density [26]. EOS–Gruneisen, EOS–linear polynomial, or EOS–tabulated models can be used to model the bird strike on the leading edge of a wing. In this study, we use the EOS–linear polynomial for the bird model to be consistent with the study of Lavoie et al. [5], which is used to validate the bird model; and its parameters are given in Sec. III.

To validate the bird model, the results of the profile of pressure between the bird and the surface, the velocity profile, and the dispersion of the bird on a plate are compared with the results from

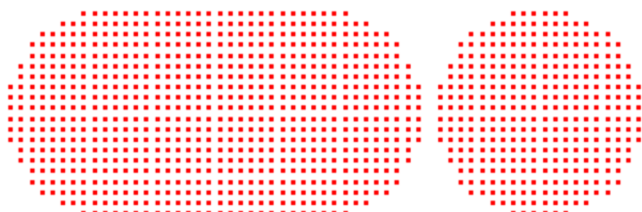


Fig. 3 Side and front views of the hemispherical-ended cylinder bird model, created with the SPH method.

existing studies in the literature. When the bird hits the target, it experiences high pressure (called the Hugoniot pressure). In Fig. 4, the peak value in zone A corresponds to the Hugoniot pressure (the initial shock regime), zone B is the pressure decay regime, zone C is the steady-state regime, and zone D is the pressure termination regime [27].

A bird strike on the wing leading edge causes plastic deformation of the edge, and failure may occur. Several material models can simulate the deformations caused by bird strikes, such as the Steinberg material model, the mechanical threshold stress material model, the Johnson–Cook material model, and the piecewise linear plasticity material model [28]. In addition to these models, the isotropic elastic–plastic model and the continuum damage mechanics model, which includes anisotropy and viscoplasticity, have been used in the literature [7,8].

To make wing leading edges more resistant to bird strikes, support structures such as sandwich panels and triangular reinforcement structures are used. Various configurations of honeycomb sandwich panels on the C27-J aircraft wing leading edge have been tested and achieved success [8,14,29]. In a different study, triangular reinforcement structures were used in an aircraft's tail leading edge to evaluate their resistance to bird strikes [12].

In this study, the impact performances of various energy-absorbent support structures integrated into the wing leading edge are evaluated. The designs should satisfy both the EASA CS-23 test standards [30] and the company's [Turkish Aerospace Industries (TAI)] requirements. The EASA standards state that an aircraft should successfully complete a flight after an impact with a 0.907 g (2 lb) bird when the aircraft's velocity relative to the bird along the aircraft's flight path equals cruise speed, which is 500 m/s (270 kt). In addition, the TAI's requirements for the wing leading-edge design are that no critical damage occurs to the front spar elements or the wing tank after impact, assuring a continued safe flight and landing. In addition to these requirements, taking a conservative approach, a scenario in which the bird does not contact the front spar element is considered successful in this study.

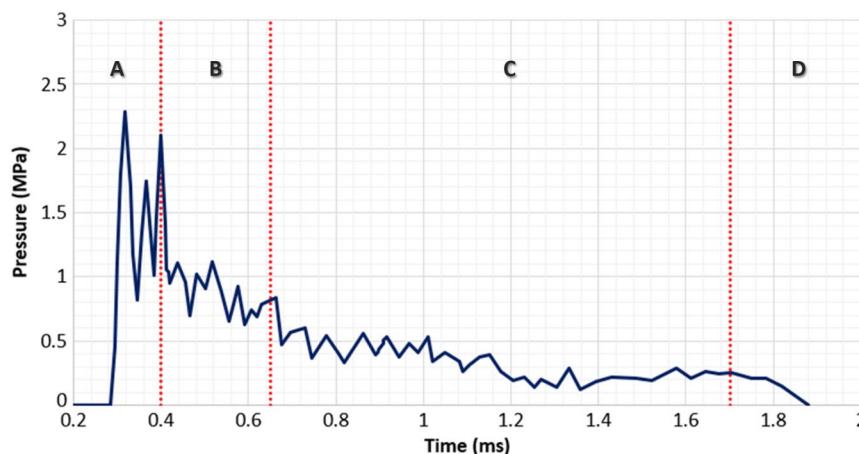


Fig. 4 Experimental pressure profile for a bird striking a rigid target at an initial velocity of 116 m/s.

III. Validation Studies

A. Validation of the Bird Model

In the literature, bird strikes on a rigid plate were analyzed using the FE method and compared with experimental data [5]. In that experiment, a 1 kg (~2.2 lb) bird impacted a $0.305 \times 0.305 \text{ m}^2$, 0.0127-m-thick fixed plate at a speed of 100 m/s. The plates used in the experiment were fixed at the edges. In the experiment, the speed of the bird projected at 100 m/s was measured to be 95 m/s during contact with the plate. Therefore, the bird velocity in the numerical study was assumed to be 95 m/s for a bird with a mass of 1 kg and a density of 950 kg/m^3 . The hemispherical-ended cylindrical bird model had a diameter of 93 mm and a length of 186 mm.

In this study, LS-DYNA software is used to predict the effects of the bird strike. Also, 10,000 hexahedral solid finite elements are used to model the plate, and 4836 particles are used to model the bird. The numbers of elements and particles are similar to those used by Lavoie et al. [5]. The plate thickness is 0.0127 m. In this study, a hemispherical cylinder geometry with a diameter of 0.093 m and length of 0.186 m was first assigned as the shell element. Subsequently, SPH particles are created over this shell element. The bird-strike analysis model used in this study is shown in Fig. 5.

The material properties are taken from the work of Lavoie et al. [5]. The target plate is rolled using homogeneous armor steel (RHA steel). LS-DYNA's MAT_ELASTIC material card is used to describe the material's properties (density of 7830 kg/m^3 , elastic modulus of 207 GPa, and Poisson's ratio of 0.3). To model the bird, MAT_ELASTIC_PLASTIC_HYDRO is used as the material card, and EOS_LINEAR_POLYNOMIAL is used as the state equation card. The material card properties are a density of 950 kg/m^3 , a shear modulus of 2 GPa, a yield strength of 20 kPa, and a plastic hardness modulus of 1 kPa; and all other parameters are set to zero. In the equation of state card, the pressure is given in Eq. (1) and the input parameters are assigned as $C_0 = C_4 = C_5 = C_6 = 0$, $C_1 = 2.06 \text{ GPa}$, $C_2 = 6.19 \text{ GPa}$, and $C_3 = 10.3 \text{ GPa}$:

$$P = C_0 + C_1\mu + C_2\mu^2 + C_3\mu^3 + (C_4 + C_5\mu + C_6\mu^2)E \quad (1)$$

where C_0-C_6 are the polynomial equation coefficients, E is internal energy, $\mu = \rho/\rho_0 - 1$, and ρ/ρ_0 is the ratio of the current density to the reference density [26].

The CONTACT_AUTOMATIC_NODES_TO_SURFACE card is used to define the contact between SPH particles and the solid elements in the analysis. FS and FD are, respectively, the static and dynamic coefficients of friction between the bird and the plate; and both are assigned a value of 0.2. SPH particles are defined in the

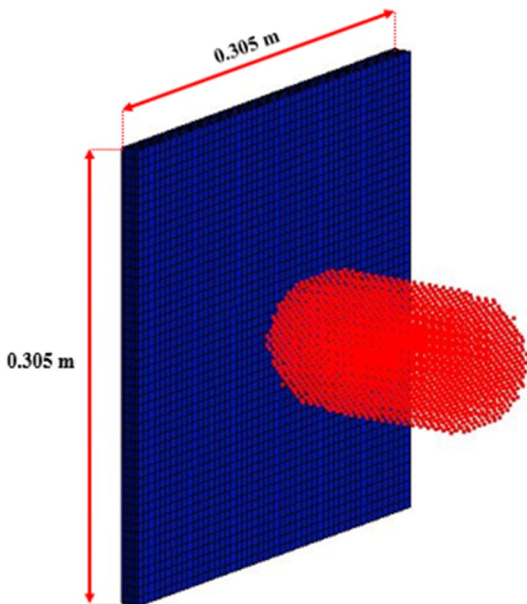


Fig. 5 The numerical model used in this study.

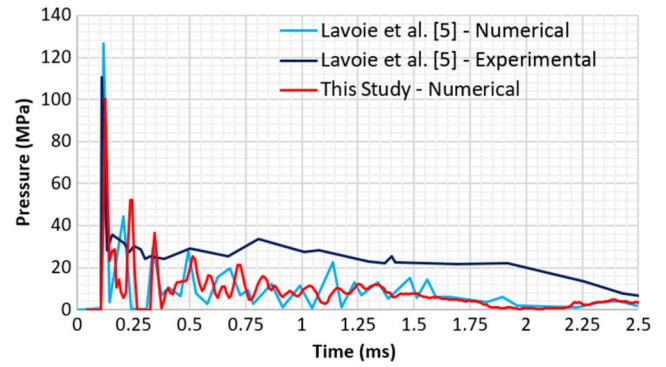


Fig. 6 Comparison of pressure readings.

slave segment set identification (SSID), and plate is defined in the master segment set identification (MSID). FE analysis generally uses slave and master when defining a contact. The reason to call it slave and master is that the slave side nodes are forced to follow the master side.

To improve simulation stability, the CONTROL_BULK_VISCOSITY card is used with parameters $Q1$ (the quadratic viscosity coefficient) equal to two and $Q2$ (the linear viscosity coefficient) equal to 0.25. Finally, for hourglass energy control, the CONTROL_HOURLASS card is used with parameters IHQ (the hourglass viscosity type) equal to two and QH (the hourglass coefficient) equal to 0.14 used, following recommendations of Hedayati and Sadighi [31].

Figure 6 shows a comparison of the pressure readings at the point where the center of the bird strikes the rigid plate at an angle of 0 deg. The numerical results of this study are consistent with both the numerical and experimental results obtained by Lavoie et al. [5] in terms of the behavior of the steady-state pressure region and the Hugoniot pressure. Figure 7 shows the variation in the velocity and diameter of the bird projectile striking at 0 deg for the experimental results and numerical models. It is observed that the results of the numerical model used in this study are consistent with the numerical model used by Lavoie et al. [5], and that both numerical models provide similar results with respect to the experimental data.

B. Validation of the Leading-Edge Model

To validate our wing leading-edge FE modeling approach, the study by Guida et al. [8], which compared the experimental and numerical leading-edge model results, is selected. Guida et al. [8] conducted a bird-strike analysis on the tail of a C27J aircraft according to the Federal Aviation Regulation 25.631, Bird Strike Damage [32]. The tail model and dimensions used in the experiment are shown in Fig. 8. According to the regulation, the bird mass must be 3.68 kg (8 lb) and impact must occur at 129 m/s on the tail leading edge.

The study of Guida et al. [8] included different configurations of skin and honeycomb thicknesses as well as different materials. In this study, the configuration that consists of a 1.4-mm-thick AA 2024 outer skin, a 6.35 mm Hexcel Flexcore honeycomb, and a 0.4-mm-thick AA 2024 inner skin is used. The honeycomb cells have been manufactured from aluminum alloy 5052 with a core cell size of 9.53 mm and a core cell wall thickness of 0.145 mm. This configuration is selected because it is the one closest to the wing leading edge evaluated in this study. In the study of Guida et al. [8], the bird model was created by modeling the cylinder geometry using the Lagrange method, and the FE analyses were performed using the MSC/Dytran FE software. The FE model of the bird and of the tail leading edge used in the work of Guida et al. [8] is shown in Fig. 9a. As noted earlier, LS-DYNA is used to predict the effects of a bird strike on the leading edge of an aircraft wing in this study. The leading-edge FE model consists of two beams, two ribs, an outer skin, a honeycomb, and an inner skin. The beams, support elements, front surface, and inner surface are formed by four-node shell elements. The honeycomb structure is composed of eight-node solid brick elements. The thickness values of the various components are as follows: beams and ribs (2 mm), outer skin surface (1.4 mm), inner skin surface (0.4 mm), and honeycomb (6.35 mm).

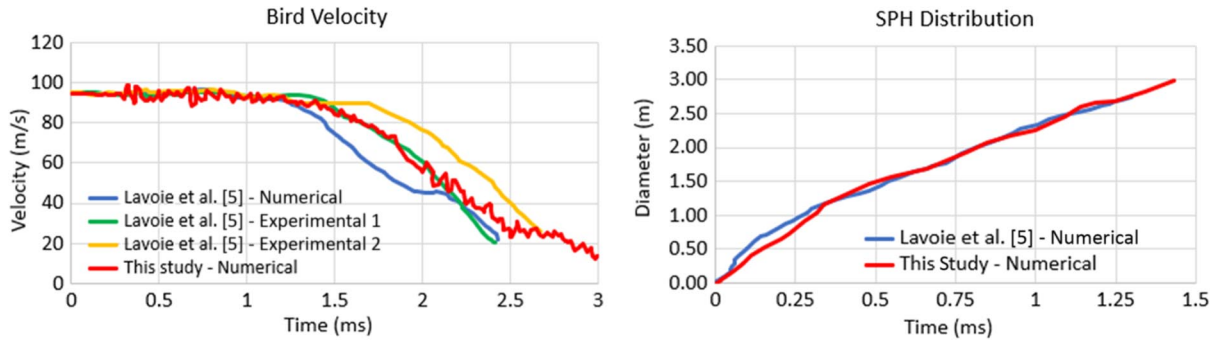


Fig. 7 Variations of the velocity (left) and diameter (right) of a projectile bird striking a steel plate at an angle of 0 deg.

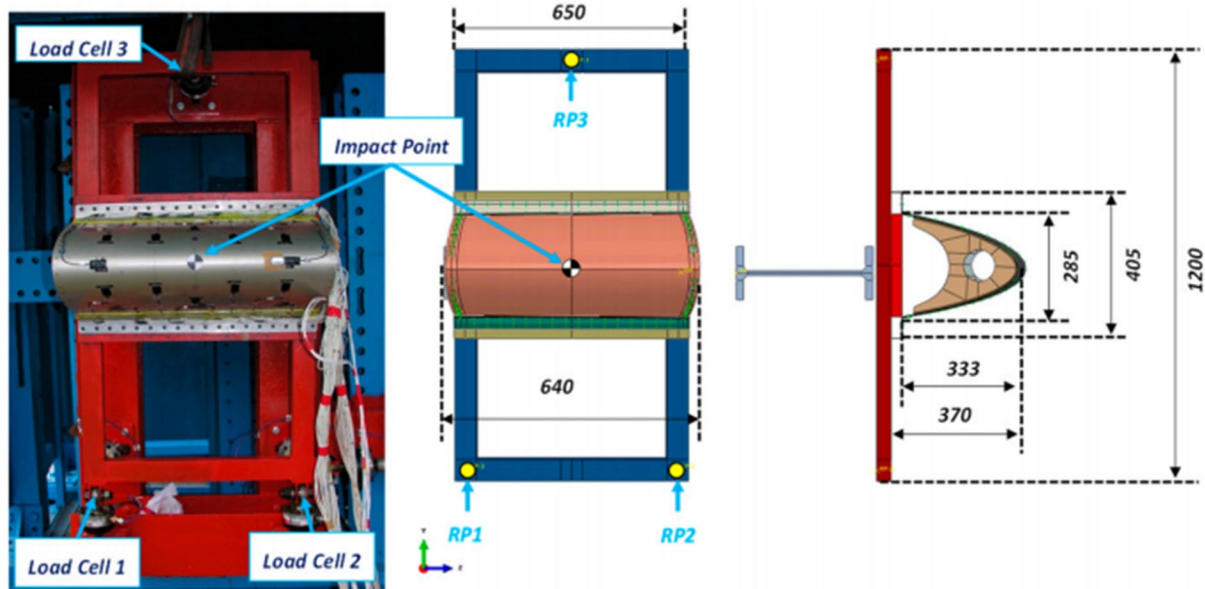


Fig. 8 Wing leading-edge model of Guida et al. [8], where dimensions are in millimeters. Reprinted in part with permission from M. Guida.

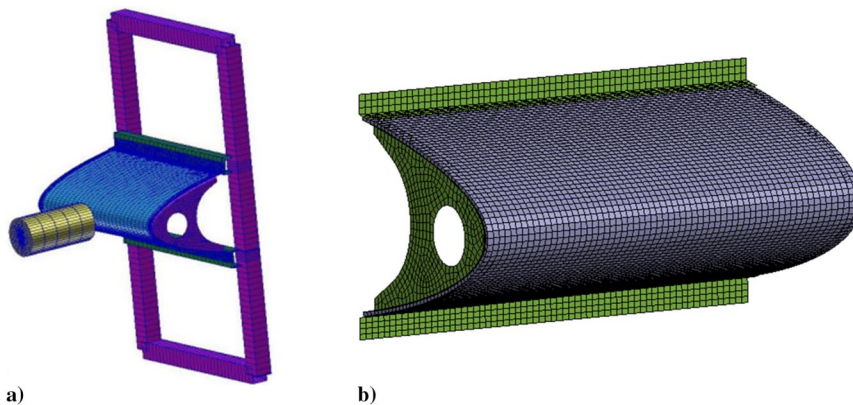


Fig. 9 Representations of a) FE model of Guida et al. [8], and b) wing leading-edge FE model. Reprinted in part with permission from M. Guida.

The inner and outer surfaces consist of 4928 elements each, the beams consist of 845 elements each, the support structures consist of 1006 elements each, and 11,707 elements are used in total to model the shell. A total of 14,400 solid elements are used to model the core structure. The beams, support elements, and outer and inner surface materials are composed of AA 2024 T3. The FE model of the leading edge is shown in Fig. 9b.

In this study, the cylinder geometry (similar to the one used by Guida et al. [8]) is used for the bird model. The bird model has a density of 946.6 kg/m^3 , measuring 134 mm in diameter and 268 mm in length; and it has a mass of 3.679 kg. The SPH method is used as the FE approach, involving 12,640 particles. The SPH particle distribution is shown in Fig. 10. Overall, a total of 29,275 elements made up the entire FE model.

The bird model cards, validated in the previous section, are used for the bird material and state equation cards. The MAT_DAMAGE_1 material model card is used for the AA 2024 T3



Fig. 10 SPH particle distribution used to model the bird body (side and front views).

Table 1 Honeycomb material properties

Properties	Value	Unit
Density	46	kg/m ³
Elastic modulus for compacted honeycomb material	0.9	GPa
Poisson's ratio for compacted honeycomb material	0.34	
Yield stress for fully compacted honeycomb	35	MPa
Relative volume at which the honeycomb is fully compacted	0.15	
Elastic modulus E_{11} in uncompressed configuration	10	MPa
Elastic modulus E_{22} in uncompressed configuration	10	MPa
Elastic modulus E_{33} in uncompressed configuration	861	MPa
Shear modulus G_{12} in uncompressed configuration.	10	MPa
Shear modulus G_{13} in uncompressed configuration.	200	MPa
Shear modulus G_{23} in uncompressed configuration.	90	MPa

material, and parameter information is taken from the work of Hanssen et al. [7], where the density of 2.77×10^{-3} g/mm³, the elastic modulus of 73.08 GPa, the Poisson's ratio of 0.33, and the yield strength of 334 MPa were used.

The MAT_MODIFIED_HONEYCOMB material model is used for the honeycomb support structure. The behavior of the uncompressed material is orthotropic. Material properties are taken from Refs. [8,14] and shown in Table 1. The stress-strain graph is defined as the lowest common ancestor graph using the DEFINE_CURVE card. The honeycomb stress-strain curve, adapted from an experimental study [8], is shown in Fig. 11a. Note that there also exist other honeycomb models in the literature [33] with different stress-strain behaviors. In this study, the honeycomb stress-strain curve taken from the work of Guida et al. [8] is used because that study is used for validation of our finite element model of the wing leading edge.

A typical stress-strain curve for the honeycomb material consists of three different regions (see Fig. 11b). The stresses are computed by dividing the compression load to a corresponding sample area, and not the area of the cell wall cross section. The honeycomb

density is computed by dividing the mass of the honeycomb to the sample volume, and not the volume of the cell walls. The first region of the curve represents the uncompacted region, and the slope of this region gives E_{unc} . In the second region of the curve, the NPR beams begin to deform. On the compacted structure, the beams are forced into contact with each other. The NPR structure is then passed to the fully completed stage, and the slope of the last region gives E_{comp} . A similar approach can also be used to obtain the shear modulus.

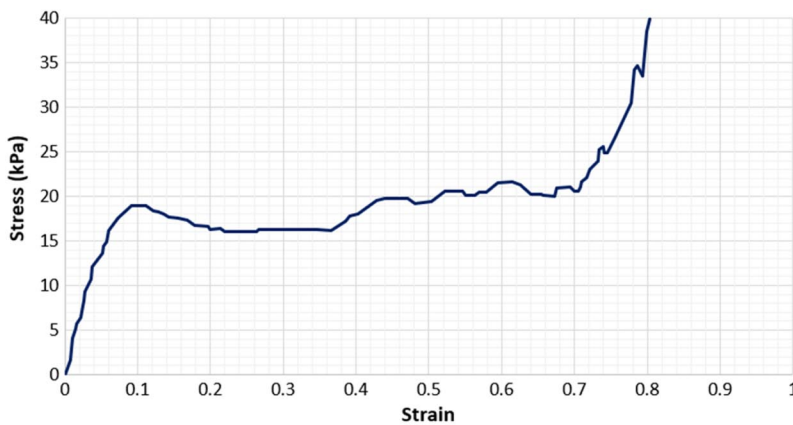
The CONTACT_AUTOMATIC_NODES_TO_SURFACE card is used to define the contact between the SPH particles and the wing surface. Owing to a possible puncture situation, a contact card for each layer of the surface with SPH particles is defined.

The CONTACT_AUTOMATIC_SINGLE_SURFACE contact card is used because the wing surface, the rib elements, and the beams are compressed after the bird impacts the wing surface. When the structure is deformed, self-contact occurs as a result of the folds that form within the material. To simulate the contact that occurs after deformation of the structure, a single surface contact algorithm is therefore applied.

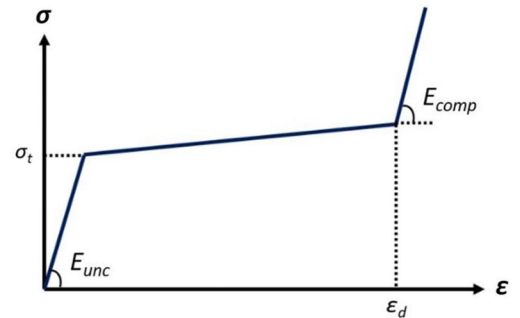
Similarly, a surface-to-surface contact algorithm is used to simulate the effect of deformed elements on each other. After the bird impacts the outer skin, the outer skin undergoes deformation. During deformation, the skin contacts other elements, such as a beam. The CONTACT_AUTOMATIC_SURFACE_TO_SURFACE contact card was used to deform the beam as a result of the contact with the outer skin. The outer surface that causes deformation during contact is defined as a slave, and the beam is defined as a master in the contact card.

The relationship between the parts connected to each other by mechanical assembly is defined by the CONTACT_TIED_SURFACE_TO_SURFACE contact card. The outer surface is connected to the beams, the support structure is connected to the outer surface, the inner surface is connected to the support structure, and the support elements are connected to the inner surface.

The center displacement on the leading edge and the displacement on the ribs between the experimental test and the numerical model are examined in this study. Figure 12a shows the change in the center

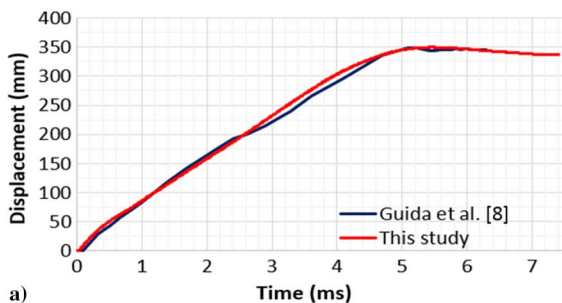


a) experimental stress-strain curve [8]

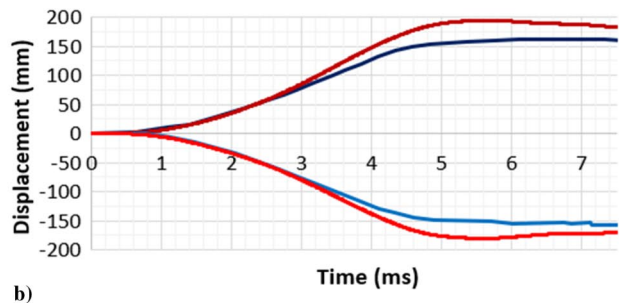


b) Typical stress-strain curve

Fig. 11 Honeycomb stress-strain curves. Reprinted in part with permission from M. Guida.



a)



b)

— Guida et al. [8] - Rib 1 — This Study - Rib 1
 — Guida et al. [8] - Rib 2 — This Study - Rib 2

Fig. 12 Displacements of a) center node and b) edge ribs.

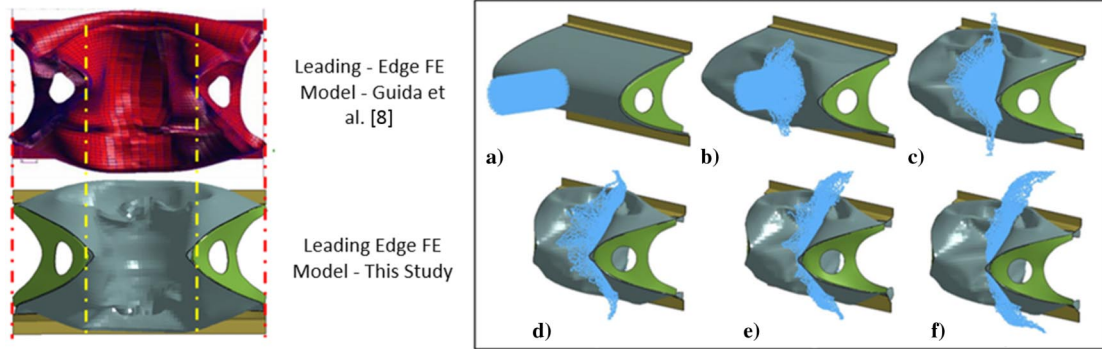
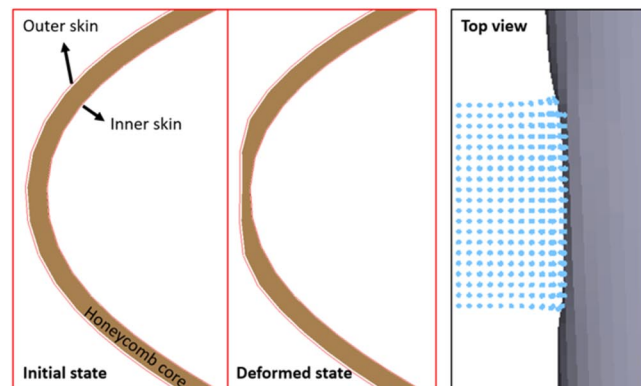


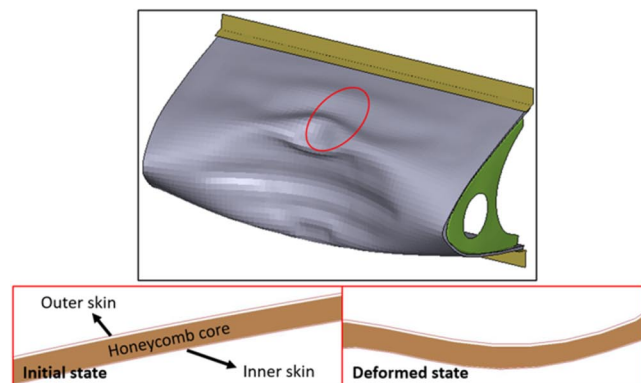
Fig. 13 Deformation comparison between leading-edge FE model and impact sequence at 1.5 ms intervals, beginning at $t_a = 0$ ms.

point in the collision zone over time, and the results of this study are close to those obtained by Guida et al. [8]. Figure 12a also shows that the maximum displacement value is consistent with the 350 mm value measured in the experimental result. Figure 12b shows that the variation in the displacement of the edge ribs over time is also consistent with the results obtained by Guida et al. [8]. Finally, Fig. 13 shows that the postcollision deformation of the ribs and wing obtained in this study are also consistent with the results obtained by Guida et al. [8].

Sandwich structures have some failure modes, depending on the loading conditions, the properties of the skin and core materials, and the geometry of the structure. Compressive loads in the sandwich plane can cause compression fracture, face wrinkling, shear crimping, and global buckling. Core failures like shear failure or local indentation can occur due to bending loads in the sandwich structure [34,35]. At the first instances of the collision, core crushing occurs in



a) Core crushing: the first moments of the collision



b) Buckling: moments during the collision

Fig. 14 Cross-section views of failure modes of the honeycomb sandwich structure: a) core crushing, with the first instances of the collision; and b) global buckling, during the collision.

the sandwich structure, as shown in Fig. 14a. During the collision, the compressive loads transmitted from front edge cause buckling failure on the upper and lower sides of the leading edge, as shown in Fig. 14b.

These core failures are very important for the energy absorption of the honeycomb core. The outer skin, inner skin, and honeycomb core have masses of 1.915, 0.533, and 0.142 kg; and the corresponding energy absorption values are 11.787, 3.542, and 3.073 kJ, respectively. Specific energy absorption is more important for the aviation industry, for which the weight has critical importance. The outer skin, inner skin, and honeycomb have 6.16, 6.65, and 21.64 kJ/kg specific energy absorption values, respectively.

IV. Case Study

After validating our bird model and the wing leading-edge model, we focus on our specific application study. In this application study, the wing leading-edge geometry provided by TAI is used (see Fig. 15). According to TAI's wing structural design experiences, the proper thickness value for the outer skin should be between 1.0 and 1.6 mm. The wing skin material is AA 2024 T3, and the front spar material is AA 2024 T42. The thickness of the front spar is 2 mm. In this study, the leading-edge design is assumed to be successful if there is no contact on the front spar element after impact. This success criterion is based on the CS-23 requirements and TAI's wing design practices. Note that in addition to this impact performance requirement, we seek to minimize the wing mass.

A. Boundary Conditions

Three-degree-of-freedom (3-DOF) displacement constraints are used at the beginning and end points of the wing sections. Additionally, six-degree-of-freedom (6-DOF) displacement and rotation constraints are imposed on the parts of the front spar that connect with the body elements. The boundary conditions are shown in Fig. 16. The remainder of the leading edge is assumed to provide a fixed boundary condition. This assumption provides a more conservative condition because energy absorption of the front spar element is not taken into account.

B. Leading-Edge Configurations

In this study, various leading-edge configurations are evaluated. First, we consider a hypothetical configuration that does not have any reinforcement in Sec. IV.B.1. Next, we consider a tradition rib design configuration in Sec. IV.B.2, followed by a honeycomb structure configuration in Sec. IV.B.3. Then, a triangular reinforcement structure configuration is taken into account in Sec. IV.B.4, followed by a modified structures configuration in Sec. IV.B.5. The depictions of these configurations are provided in Fig. 17. Finally, an NPR honeycomb structure configuration is considered in Sec. IV.B.6.

1. Outer-Surface-Only Configuration

This configuration, shown in Fig. 17a, is used to determine the minimum thickness required so that the outer surface can withstand a bird strike when there is no additional support structure. In this

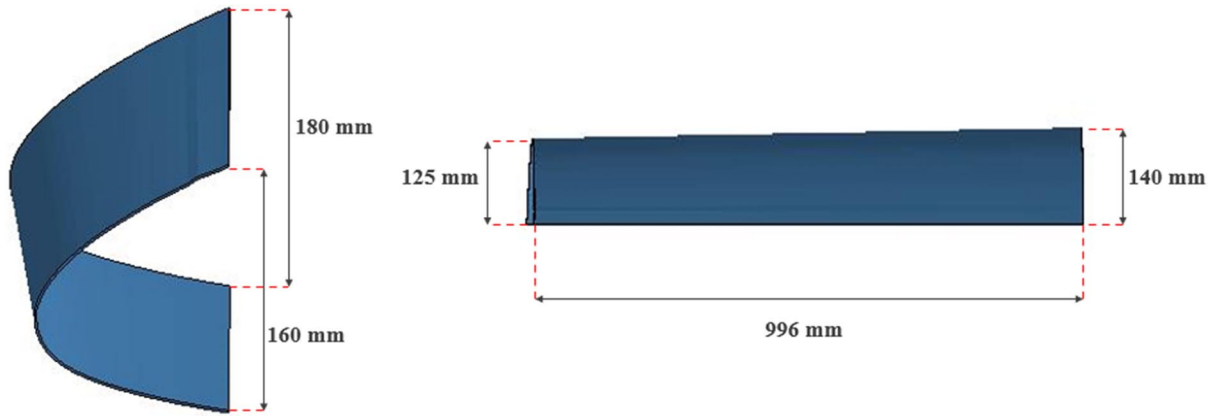


Fig. 15 Wing leading-edge geometry considered in this study.

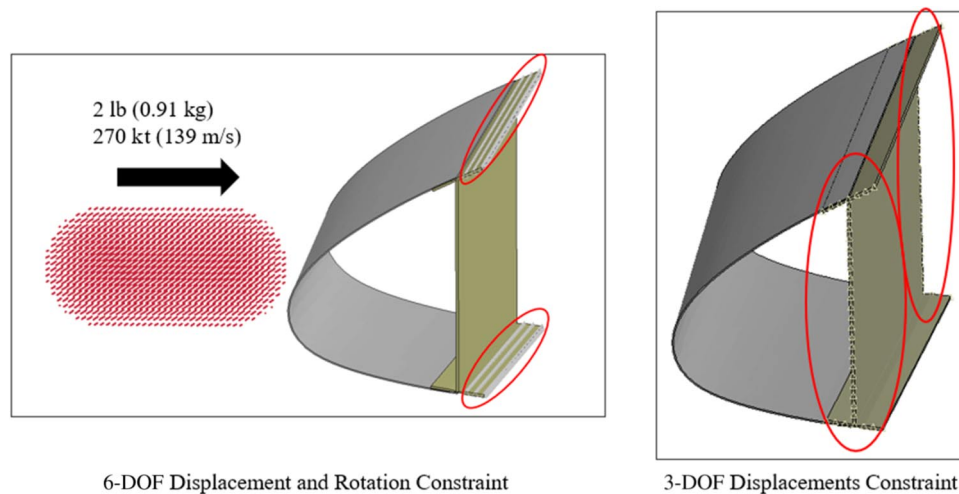


Fig. 16 Boundary conditions.

configuration, different outer skin thickness values are analyzed. The outer skin material used is AA 2024 T3. The minimum thickness value satisfying the CS-23 requirements is found to be 1.85 mm. Obviously, this configuration is a hypothetical one, and the required skin thickness is quite high.

2. Traditional Rib Design Configuration

This configuration, shown in Fig. 17b, is used to evaluate the behavior of the classic rib design used in certifications. The material of the ribs is AA 2024 T3. There are six ribs on the wing leading-edge part analyzed. The ribs are set 200 mm apart from each other. In this case, the rib thickness is 2 mm, and all ribs are 20 mm wide. Two collision scenarios in the impact zone are examined. In the first condition, the bird impacts directly on a rib. In the second condition, the bird impacts in the middle between two ribs.

3. Honeycomb Structure Configuration

In this configuration, shown in Fig. 17c, Hexcel Company's HexWeb® Aluminum 5052 Flex-Core® 6.35 mm product is used, where AA 2024T3 is used as the inner and outer panel material. In this configuration, the thickness of the outer skin is 1.2 mm, the honeycomb thickness is 6.35 mm, and the inner skin thickness is 0.4 mm. A mounting interface is used to mount the panels to the front spar element. The mounting interface material is AA 2024 T3.

4. Triangular Reinforcement Structure Configuration

This configuration is inspired by the works of Liu et al. [12] and Yu et al. [36], where a triangular reinforcement structure (TRS) was used. A TRS is intended to deflect a bird rather than absorb the full impact energy. Considering weight, the traditional TRS is heavier

than other configurations. Therefore, three different configurations are considered in this study for the triangular support structures to evaluate possible weight reduction designs. AA 2024 T3 is used as the TRS material in all subconfigurations.

a. Traditional TRS Subconfiguration. The first subconfiguration, named the traditional TRS configuration in this study, is a traditionally designed triangular support structure. Different outer skin and TRS thickness values are evaluated using the traditional TRS configuration. Three outer skin thickness values (namely, 1.0, 1.3, and 1.6 mm) are taken into account, and the smallest TRS thickness value that satisfies the CS-23 requirements is determined, corresponding to each outer thickness value, as listed in Table 2. The traditional TRS configuration is shown in Fig. 17d.

b. Topological TRS Subconfiguration. In the second subconfiguration, shown in Fig. 17e, regions showing low stress values under load conditions are removed from the structure through topology optimization using the LS-DYNA topology optimization tool [26]. Using the mass and velocity of the bird, the impact force is first calculated. Then, a region equal to the size of the bird is taken from the support structure, and the topology optimization is performed on the limited region by applying the determined force. As a result of the obtained topology optimization, the final geometry is replicated periodically over the entire wing. This subconfiguration is called the topological TRS configuration. The thickness values determined for the lightest structure that meets CS-23 requirements are listed in Table 3.

c. Topometric TRS Subconfiguration. In the third subconfiguration, shown in Fig. 17f, a topometric study is carried out to reduce the

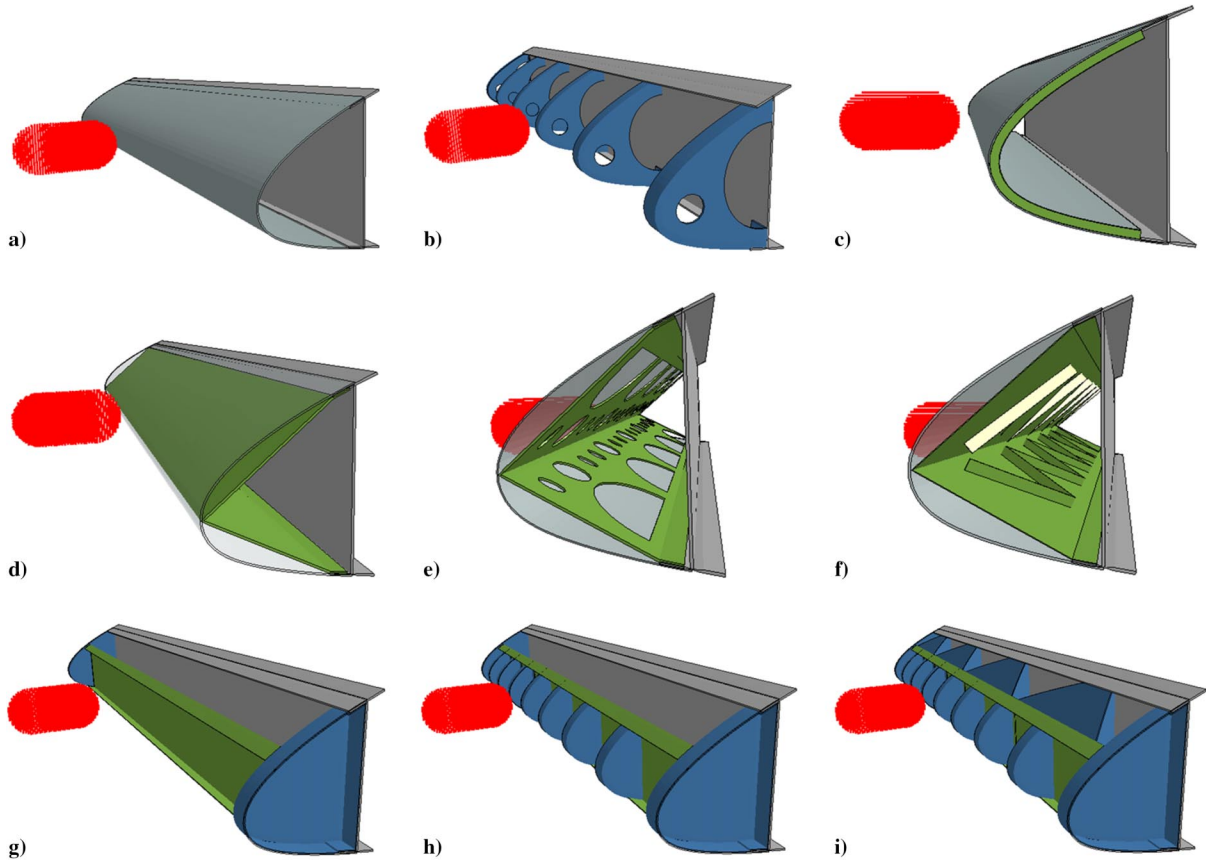


Fig. 17 Configurations: a) outer-surface-only, b) traditional rib design, c) honeycomb sandwich structure, d) traditional TRS, e) topological TRS, f) topometric TRS, g) modified structure with subspar, h) modified structure with front rib, and i) modified structure with rear rib.

Table 2 Thicknesses of various traditional TRS configurations

Configurations	Outer skin thickness, mm	TRS thickness, mm
Traditional TRS 1.0	1.0	1.05
Traditional TRS 1.3	1.3	0.85
Traditional TRS 1.6	1.6	0.58

Table 3 Thicknesses of various topological TRS thickness configurations

Configurations	Outer skin thickness, mm	TRS thickness, mm
Topological TRS 1.0	1	1.75
Topological TRS 1.6	1.6	0.96

thickness of the TRS while maintaining its rigidity. This subconfiguration is called the topometric TRS configuration. In this subconfiguration, stringers are added to prevent surface buckling. Topometric support structures are added to regions showing high stress values under load conditions in the structure. These regions are determined by following the same approach as explained in the topological subconfiguration. The topometric support structures have the same thickness as the TRS thickness in all configurations. The smallest thickness values that meet CS-23 requirements are listed in Table 4.

Table 4 Thicknesses of various topometric TRS thickness configurations

Configurations	Outer skin thickness, mm	TRS thickness, mm
Topometric TRS 1.0	1.0	0.875
Topometric TRS 1.3	1.3	0.750
Topometric TRS 1.6	1.6	0.400

5. Modified Structures Configuration

This configuration is inspired by Kumar's study [37], where modified structures were used. The modified structures are created by changing the structure and configuration of traditional support elements. The developed structures include three different subconfigurations, and AA 2024 T3 is used as the material for all added support structures.

a. Modified Structure with Subspar Configuration. In the first subconfiguration, the support structure consists of two side ribs and one subspar in the configuration, and the subspar is placed 75 mm from the front spar. The outer skin and side rib thickness is 1 mm, and the subspar thickness is 2.5 mm. The modified structure with a subspar is shown in Fig. 17g.

b. Modified Structure with Front Rib Configuration. In the second subconfiguration, seven front ribs are added in addition to the subspar. Ribs are placed 125 mm apart, and each rib measures 20 mm in width. The thickness of the outer skin, front ribs, and side ribs is 1 mm; and the thickness of the subspar is 1.75 mm. The thickness values are determined for the lightest structure that meets CS-23 requirements. The modified structure with front ribs is shown in Fig. 17h.

c. Modified Structure with Rear Rib Configuration. In the third subconfiguration, eight ribs are placed between the front spar and the subspar. Each rear rib is 250 mm wide. Here, the thickness of the outer skin, side ribs, front ribs, and subspar is 1 mm. The modified structure with the rear rib configuration is shown in Fig. 17i.

6. Negative Poisson's Ratio Structure Configuration

There exist various NPR types according to their cellular structures, including reentrant, chiral, and rotating units. In this study, a reentrant NPR structure is used, following the work of Wang et al.

[16]. As noted earlier, we propose the use of NPR structures as wing leading-edge support structures for the first time in the literature (to the best of our knowledge). Two subconfigurations are considered, as will be detailed in the subsequent sections.

a. NPR Subspar Configuration. In this first subconfiguration, called the NPR subspar configuration, a reentrant NPR structure (see Fig. 18) is placed between the spar elements in the wing leading-edge configuration. When defining cell dimensions, the height of the cell is represented by h , the edge length of the cell is l , the edge thickness of the cell is t , and the θ parameter is used to indicate the angle of the cell's edge to the vertical axis.

The NPR structure used on the wing leading edge consists of $3 \times 3 \times 31$ cells. A cell's height and edge length are $h = 20$ mm and $l = 10$ mm, respectively. The thickness of the edge is assigned as $t = 1.2$ mm. The cell wall angle is $\theta = 30$ deg, and AA 2024 T3 is used as the NPR structure material. The representative cell structure is shown in Fig. 19. In the NPR subspar configuration, the outer skin thickness is 1 mm; and the thicknesses of the front subspar and middle subspar are 0.7 and 1.2 mm, respectively. Figure 20 shows the leading edge of the wing with the NPR structure. The NPR structure in this subconfiguration is found to be insufficient for energy absorbing due to a narrow collision zone and a low number of cells. Therefore, the size of the unit cell is reduced and placed on the leading edge as a sandwich structure like a honeycomb in the next subconfiguration.

b. NPR Honeycomb Configuration. In this subconfiguration, called the NPR honeycomb configuration, the structure with the same height (6.35 mm) as that of the earlier honeycomb structure (discussed earlier in Sec. IV.B.3) is created. Note that the leading edge with the NPR honeycomb configuration is the same as the leading edge with the honeycomb sandwich structure used earlier (see Fig. 17c), except that the honeycomb material properties are different.

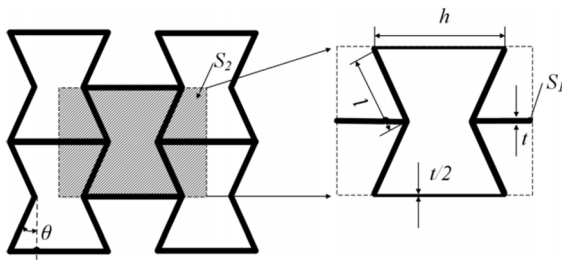


Fig. 18 NPR geometry.

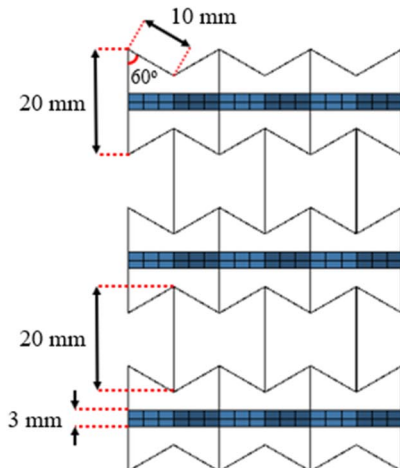


Fig. 19 NPR cell structure.

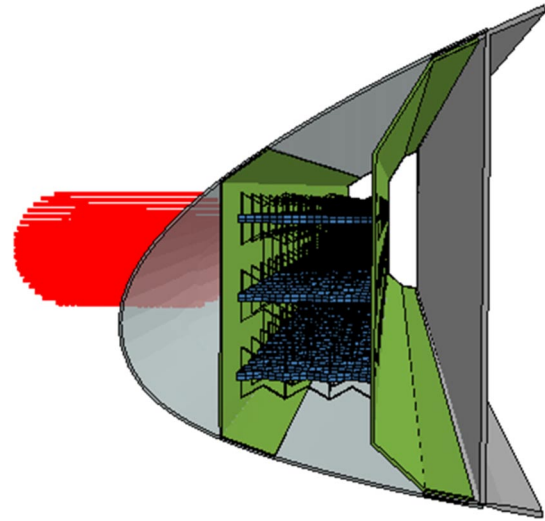


Fig. 20 Leading edge with NPR subspar configuration.

A homogenization method is used to compute the material model parameters of the NPR honeycomb structure. The MAT_MODIFIED_HONEYCOMB material model is used to characterize the elastic-plastic anisotropic behavior of the NPR structure, which consists of a cellular structure such as the honeycomb and foam [38]. To obtain the directional material properties to be used in the MAT_MODIFIED_HONEYCOMB card, a numerical (or virtual) high strain rate compression test and shear test in the L, W, and T direction are performed at the strain rate of 100 s^{-1} . Note that L direction is the ribbon direction, W direction is the direction perpendicular to the ribbon, and T direction is the thickness direction. The NPR structure used in the numerical tests had a $4 \times 4 \times 4$ cell configuration and included from 9024 to 17,536 elements.

The NPR cell geometry highly affects the strength of the structure. Different cell geometries and their performances are investigated by changing the angle of the cell's edge to the vertical axis (θ angle in Fig. 18). The θ values of 60, 45, 30, 15, 10, and 5 deg are investigated. The NPR structures in these angles are shown in Fig. 21. Also, the effect of the wall thickness values of the NPR cells is investigated, where 0.10 and 0.12 mm wall thickness values are considered.

The most dominant parameter affecting the impact performance is found to be the compression character in the L direction of the NPR. Therefore, the compression characteristics in the L direction are compared for different cell structure configurations. Figure 22 shows deformation behavior of the $\theta = 30$ deg NPR structure in the 0.10 mm wall thickness under an L direction

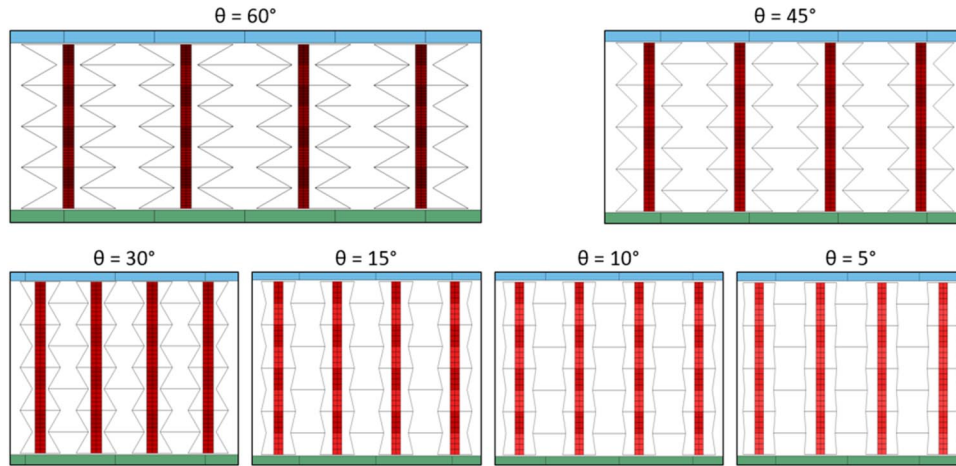


Fig. 21 NPR structures with different θ angles.

compression test until the 0.8 mm/mm strain. According to these numerical compression tests, stress–strain curves are investigated to determine the structure giving the best crash performance. Figure 23a shows the stress–strain curves for various θ angles for a 0.10 mm wall thickness, and Fig. 23b shows them for a 0.12 mm wall thickness.

By using the stress–strain graphs obtained from different directions, the compacted E_{comp} and uncompactd E_{unc} Young modulus

values for the MAT_MODIFIED_HONEYCOMB card are calculated. Based on the stress–strain curves given in Figs. 23a and 23b, it is seen that the stiffness of the structure increases when the wall thickness is increased, as expected. It is also seen that the angle of the NPR structure θ highly affects the performance. As θ decreases, the impact performance of the structure increases. When the wall thickness is set to 0.10 mm, none of the θ angles investigated could satisfy EASA CS-23 requirements. On the other hand, when the wall thick-

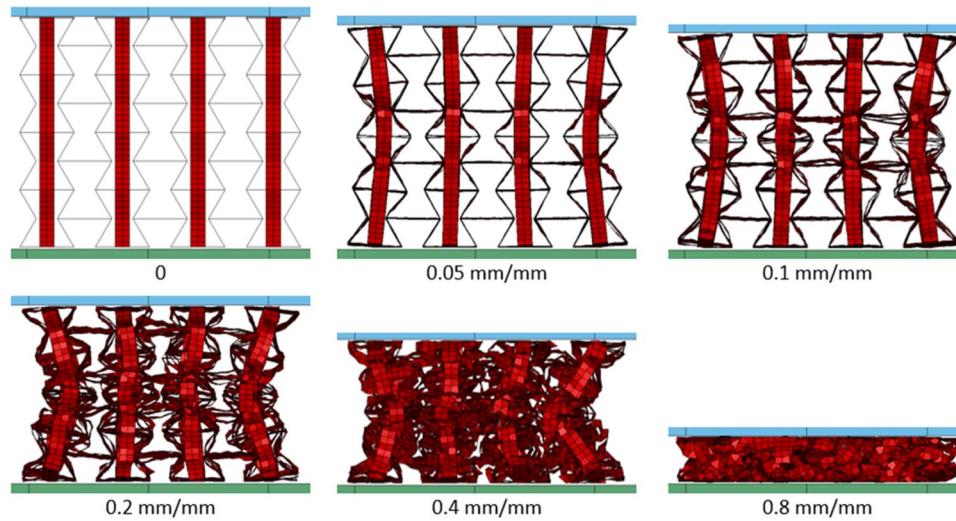


Fig. 22 Numerical L direction compression test for the NPR structure when $\theta = 30$ deg.

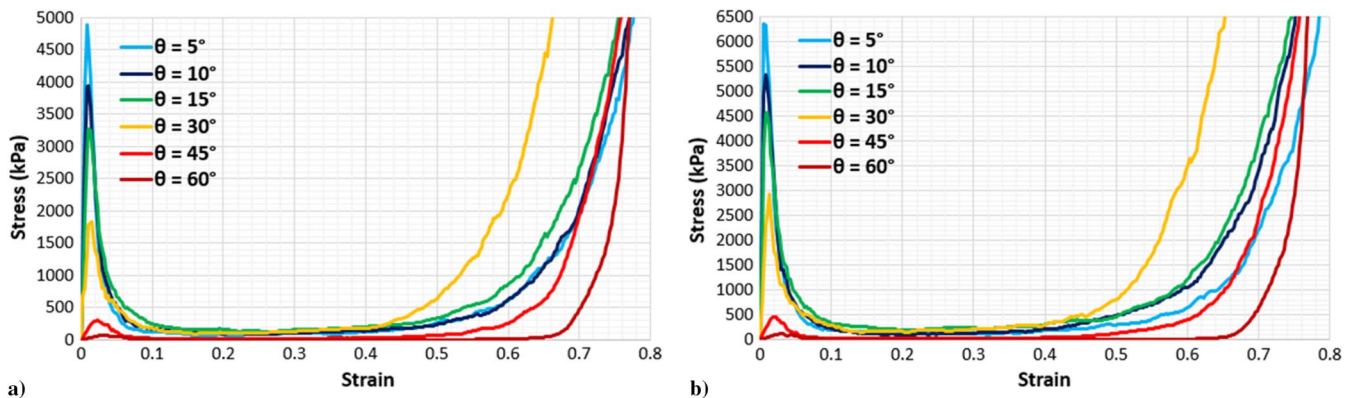


Fig. 23 Stress–strain curves for the NPR honeycomb material for various θ angles for a) 0.10 mm wall thickness, and b) 0.12 mm wall thickness.

ness is set to 0.12 mm, the $\theta = 5$ deg cell angle configuration satisfied the EASA CS-23 requirements. It is determined that the wall thickness configuration with $\theta = 5$ deg and 0.12 mm shows the best performance among all configurations.

V. Results

Table 5 lists the impact performances of the different support structure configurations considered in this study, as well as their weights. As noted earlier, the minimum weight design of the wing leading edge is sought for all these configurations such that the EASA CS-23 standards are satisfied and there is no contact on the front spar element after impact (TAI's design requirement). The rank of the support structures in Table 5 is determined according to following: first, meeting the impact requirements; and second, meeting the weight reduction goal. In addition, the maximum deformations of the support structures are given in Table 6. The following are observed from the results provided in Tables 5 and 6:

1) The best impact performance and lowest weight are achieved when the honeycomb support structure is used.

2) Interestingly, the second-best performance is achieved by the "outer-surface-only" configuration using a thickness of 1.85 mm, resulting in a 3.082 kg weight.

3) For the TRS configurations, the outer skin thicknesses of 1 mm (TRS 1), 1.3 mm (TRS 1.3), and 1.6 mm (TRS 1.6) all satisfy the impact requirements. Because TRS 1 has less weight than both TRS 1.3 and TRS 1.6, Table 5 includes only the TRS 1 type for traditional, topological, and topometric configurations.

4) The topometric TRS shows the best performance among the TRS configurations, whereas the topological TRS shows the worst performance.

5) In the traditional rib design, two different configurations related to the collision zone are examined. Damage occurs to the front spar element in both configurations because the outer skin is torn during impact, as can be seen in Table 6. The main reason for this behavior is that the ribs behave rigidly and do not deform and absorb energy during a collision. Because the front spar is affected during the collision, both configurations fail to satisfy the impact requirement.

6) For the modified structure subspare configuration, the weight of the lightest structure that provides acceptable crash performance is 3.648 kg.

7) Although the thickness of the support structures is increased in the modified structure with the rear rib configuration, it does not meet the impact requirements, even though its weight of 3.469 kg would be acceptable. With the absence of rear ribs and increased subspare thickness, the modified structure front rib configurations meet the EASA CS-23 requirements.

8) The NPR subspare configuration does not meet impact requirements because of the narrow collision zone created by the configuration. The NPR honeycomb configuration, on the other hand, satisfies the impact requirements; and the best NPR honeycomb configuration is obtained when the angle is $\theta = 5$ deg and the wall

thickness is 0.12 mm, resulting in a wing leading-edge weight of 3.393 kg.

VI. Conclusions

In this study, the effects of a bird strike on the leading edge of the wing of a training aircraft were investigated in accordance with EASA CS-23 standards. After validating bird and wing leading-edge FE models, various design options were compared for energy-absorbing support structures applicable to the leading-edge geometry provided by TAI in terms of their impact performance and weight.

First, a design without a support structure (a hypothetical case) was considered, and the value of the outer skin thickness that would provide sufficient protection against bird strikes on the leading edge was determined. An outer skin thickness of 1.85 mm was found to provide satisfactory protection and is lighter than all designs using support structures, except for the honeycomb support structure. However, considering the different loads and vibration that may occur during multiple flights, this hypothetical design may not be preferred.

Among all the support structure configurations examined in this study, the honeycomb support structure performed best in terms of impact resistance and weight. Considering other support structures, topometric and topological TRS configurations performed well in terms of weight.

The TRS is intended to deflect a bird rather than absorb the full impact energy at the time of collision. Among the configurations, increasing the TRS thickness to 1.6 mm provided the best performance, and the topometric TRS achieved the best results among the TRS configurations evaluated. It was observed that the topometric TRS maintained its rigidity during impact. Owing to its rigidity, it created a beneficial knife effect on the bird at the time of collision. This knife effect decreased as the TRS thickness decreased. The knife effect of the TRS can be seen in the isometric views in Table 6.

The weight of the topometric TRS design is close to the outer-surface-only design. Some modifications such as the use of different thickness values for the stringers and the support structure can be performed in the topometric TRS to improve its performance.

Modified structures were created using different combinations of traditional support structures. For the modified structures examined, the energy absorbance values increased, depending on the thickness of the subspare and outer skin. It was observed that designs with rear ribs and front ribs were not efficient absorbers.

This study presented analysis of NPR structures as support structures for the wing leading edge for the first time in the literature, to the best of the authors' knowledge. The NPR subspare configuration did not meet impact requirements because of the narrow collision zone created by the configuration. The NPR honeycomb configuration, on the other hand, was observed to satisfy the impact requirements when the proper angle and wall thickness values were used. It was also noted that the NPR honeycomb configuration was not very weight efficient. Further research could be conducted to improve its weight efficiency.

Table 5 Support structures ranked based on weight goal and impact performance, where impact requirements include both EASA CS-23 standards and TAI's requirements

Rank	Support structures	Total weight,kg	Meets impact requirements?
1	Honeycomb	2.961	Yes
2	Outer surface only	3.082	Yes
3	Topometric TRS 1.0	3.103	Yes
4	Traditional TRS 1.0	3.185	Yes
5	Topological TRS 1.0	3.300	Yes
6	Modified structure front rib configuration	3.336	Yes
7	NPR honeycomb configuration	3.393	Yes
8	Modified structure subspare configuration	3.648	Yes
9	Traditional rib design	3.418	No
10	Modified structure rear rib configuration	3.469	No
11	NPR subspare configuration	3.788	No

Table 6 Maximum deformations of the support structures

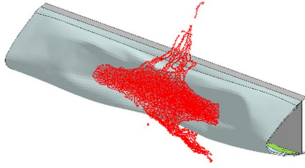
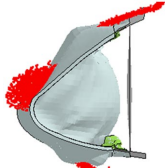
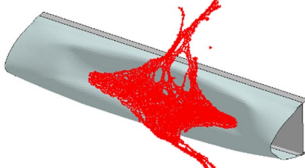
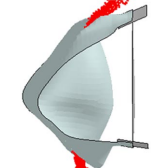
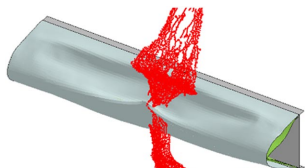
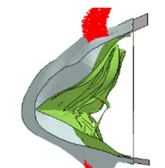
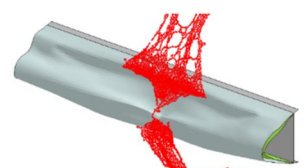
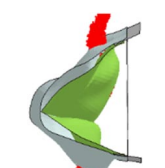
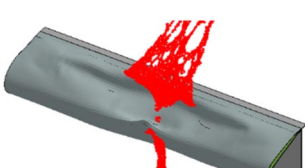
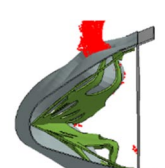
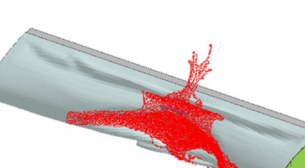
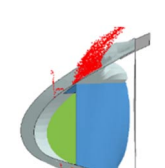
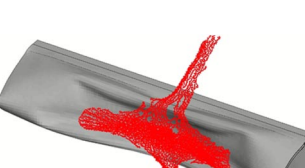

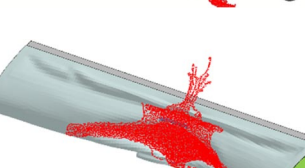
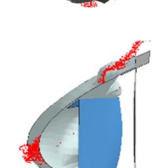
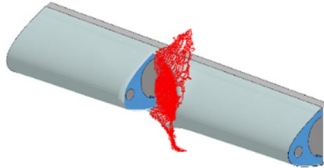
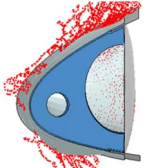
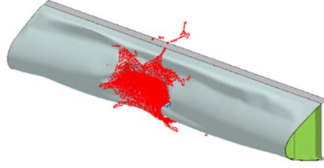
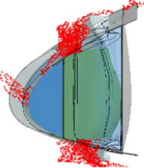
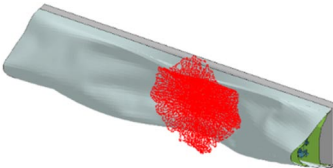
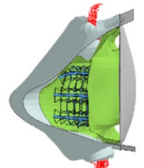
Support structures	Isometric view	Side view
1) Honeycomb		
2) Outer surface only		
3) Topometric TRS		
4) Traditional TRS		
5) Topological TRS		
6) Modified structure front rib configuration		
7) NPR honeycomb configuration		
8) Modified structure subspar configuration		

Table 6 (Continued.)

Support structures	Isometric view	Side view
9) Traditional rib design		
10) Modified structure rear rib configuration		
11) NPR subspar configuration		

Acknowledgments

This study was supported by the Scientific and Technological Research Council of Turkey (TUBITAK) project no. 20AG027 under program no. 20AG001, the TUBITAK Bilim İnsanı Destek Programları Başkanlığı (BİDEB) 2209-B Undergraduate Research Project Support Program for Industry 2020/1, and the Turkish Aerospace Industry under the Lift-Up Program 2020/2021.

References

- [1] Metz, I. C., Ellerbroek, J., Mühlhausen, T., Kügler, D., and Hoekstra, J. M., "The Bird Strike Challenge," *Aerospace*, Vol. 7, No. 3, 2020, Paper 26.
<https://doi.org/10.3390/aerospace7030026>
- [2] Dolbeer, R. A., Begier, M. J., Miller, P. R., Weller, J. R., and Anderson, A. L., "Wildlife Strikes to Civil Aircraft in the United States, 1990–2019," Rept. DOT/FAA/TC-21/11, U.S. Dept. of Transportation, Federal Aviation Administration, William J. Hughes Technical Center, 2021.
- [3] Li, J., Lou, Y., Chai, X., Ma, Z., and Jin, X., "Numerical Simulation of Bird Strike on Jet Engine Considering Bird Ingestion Requirements," *Journal of Aircraft*, Vol. 59, No. 3, 2021, pp. 1–13.
<https://doi.org/10.2514/1.C036076>
- [4] Barber, J. P., Taylor, H. R., and Wilbeck, J. S., "Characterization of Bird Impacts on a Rigid Plate," US Air Force Flight Dynamics Lab. TR-75-5, 1975.
<https://doi.org/10.21236/ada021142>
- [5] Lavoie, M. A., Gakwaya, A., Ensan, M. N., Zimcik, D. G., and Nandlall, D., "Bird's Substitute Tests Results and Evaluation of Available Numerical Methods," *International Journal of Impact Engineering*, Vol. 36, Nos. 10–11, 2009, pp. 1276–1287.
<https://doi.org/10.1016/j.ijimpeng.2009.03.009>
- [6] Shupikov, A. N., Ugrimov, S. V., Smetankina, N. V., Yareshchenko, V. G., Onhirskey, G. G., Ukolov, V. P., and Avramenko, V. L., "Bird Dummy for Investigating the Bird-Strike Resistance of Aircraft Components," *Journal of Aircraft*, Vol. 50, No. 3, 2013, pp. 817–826.
<https://doi.org/10.2514/1.C032008>
- [7] Hanssen, A. G., Girard, Y., Olovsson, L., Berstad, T., and Langseth, M., "A Numerical Model for Bird Strike of Aluminium Foam-Based Sandwich Panels," *International Journal of Impact Engineering*, Vol. 32, No. 7, 2006, pp. 1127–1144.
<https://doi.org/10.1016/j.ijimpeng.2004.09.004>
- [8] Guida, M., "Study, Design and Testing of Structural Configurations for the Bird-Strike Compliance of Aeronautical Components," Ph.D. Thesis, Aerospace Engineering Dept., Univ. of Naples "Federica II", Naples, Italy, Dec. 2008.
- [9] Guida, M., Marulo, F., Polito, T., Meo, M., and Riccio, M., "Design and Testing of a Fiber-Metal-Laminate Bird-Strike-Resistant Leading Edge," *Journal of Aircraft*, Vol. 46, No. 6, 2009, pp. 2121–2129.
<https://doi.org/10.2514/1.43943>
- [10] Smojver, I., and Ivančević, D., "Numerical Simulation of Bird Strike Damage Prediction in Airplane Flap Structure," *Composite Structures*, Vol. 92, No. 9, 2010, pp. 2016–2026.
<https://doi.org/10.1016/j.compstruct.2009.12.006>
- [11] Zhang, C., Binienda, W. K., Horvat, F. E., and Wang, W., "Application of Numerical Methods for Crashworthiness Investigation of a Large Aircraft Wing Impact with a Tree," *Mathematical and Computational Forestry and Natural-Resource Sciences*, Vol. 5, No. 1, 2013, pp. 71–85.
- [12] Liu, J., Li, Y., Yu, X., Tang, Z., Gao, X., Lv, J., and Zhang, Z., "A Novel Design for Reinforcing the Aircraft Tail Leading Edge Structure Against Bird Strike," *International Journal of Impact Engineering*, Vol. 105, July 2017, pp. 89–101.
<https://doi.org/10.1016/j.ijimpeng.2016.12.017>
- [13] Liu, J., Li, Y., Yu, X., Gao, X., and Liu, Z., "Design of Aircraft Structures Against Threat of Bird Strikes," *Chinese Journal of Aeronautics*, Vol. 31, No. 7, 2018, pp. 1535–1558.
<https://doi.org/10.1016/j.cja.2018.05.004>
- [14] Di Caprio, F., Cristillo, D., Saputo, S., Guida, M., and Riccio, A., "Crashworthiness of Wing Leading Edges Under Bird Impact Event," *Composite Structures*, Vol. 216, May 2019, pp. 39–52.
<https://doi.org/10.1016/j.compstruct.2019.02.069>
- [15] Arachchige, B., Ghasemnejad, H., and Yasaei, M., "Effect of Bird-Strike on Sandwich Composite Aircraft Wing Leading Edge," *Advances in Engineering Software*, Vol. 148, Oct. 2020, Paper 102839.
<https://doi.org/10.1016/j.advengsoft.2020.102839>
- [16] Wang, T., An, J., He, H., Wen, X., and Xi, X., "A Novel 3D Impact Energy Absorption Structure with Negative Poisson's Ratio and Its Application in Aircraft Crashworthiness," *Composite Structures*, Vol. 262, April 2021, Paper 113663.
<https://doi.org/10.1016/j.compstruct.2021.113663>
- [17] Gao, Q., Zhao, X., Wang, C., Wang, L., and Ma, Z., "Multi-Objective Crashworthiness Optimization for an Auxetic Cylindrical Structure Under Axial Impact Loading," *Materials and Design*, Vol. 143, April 2018, pp. 120–130.
<https://doi.org/10.1016/j.matdes.2018.01.063>
- [18] Heimbs, S., "Computational Methods for Bird Strike Simulations: A Review," *Computers and Structures*, Vol. 89, Nos. 23–24, 2011, pp. 2093–2112.
<https://doi.org/10.1016/j.compstruc.2011.08.007>

- [19] Gakwaya, A., and Ensan, M. N., "Validation of Available Approaches for Numerical Bird Strike Modeling Tools," *International Review of Mechanical Engineering*, Vol. 1, No. 4, 2007, pp. 380–389.
- [20] Anghileri, M., Castelletti, L. M. L., and Mazza, V., "Birdstrike: Approaches to the Analysis of Impacts with Penetration," *International Conference on Impact Loading of Lightweight Structures, WIT Transactions on Engineering Sciences*. 2005.
- [21] McCallum, S. C., and Constantinou, C., "The Influence of Bird-Shape in Bird-Strike Analysis," *5th European LS-DYNA Users Conference*, Birmingham. 2005.
<https://doi.org/10.2991/cisia-15.2015.267>
- [22] Nizampatnam, L., and Holzapfel, M., "Modelling Soft Body Impact on Composite Structures," *Composite Structures*, Vol. 61, Nos. 1–2, 2003, pp. 103–113.
[https://doi.org/10.1016/S0263-8223\(03\)00033-3](https://doi.org/10.1016/S0263-8223(03)00033-3)
- [23] Nizampatnam, L., and Horn, W., "Investigation of Equation of State Models for Predicting Bird Impact Loads," *46th AIAA Aerospace Sciences Meeting and Exhibit*, AIAA Paper 2008-682, 2008.
<https://doi.org/10.2514/6.2008-682>
- [24] Hedayati, R., and Ziaei-Rad, S., "New Bird Model for Simulation of Bird Strike on Various Layups Used in Transparent Components of Rotorcrafts," *Journal of Aerospace Engineering*, Vol. 27, No. 1, 2014, pp. 76–85.
[https://doi.org/10.1061/\(ASCE\)AS.1943-5525.0000225](https://doi.org/10.1061/(ASCE)AS.1943-5525.0000225)
- [25] Hedayati, R., and Sadighi, M., *Bird strike: An Experimental, Theoretical and Numerical Investigation*, Woodhead Publ., Sawston, England, U.K., 2015.
- [26] *LS-DYNA Theory Manual*, Livermore Software Technology Corp., Livermore, CA, 2007.
- [27] Hedayati, R., Sadighi, M., and Mohammadi-Aghdam, M., "On the Difference of Pressure Readings from the Numerical, Experimental and Theoretical Results in Different Bird Strike Studies," *Aerospace Science and Technology*, Vol. 32, No. 1, 2014, pp. 260–266.
<https://doi.org/10.1016/j.ast.2013.10.008>
- [28] Dede, O., "Investigation of Effects of Bird Strike on Wing Leading Edge by Using Explicit Finite Element Method," MSc Thesis, Dept. of Aerospace Engineering, Middle East Technical Univ., Ankara, Turkey, 2015.
- [29] Belkhef, F. Z., and Boukraa, S., "Damage Prediction and Test Validation of Bird Impacts on Aircraft Leading Edge's Structures," *International Journal of Crashworthiness*, Vol. 27, No. 3, 2020, pp. 1–18.
<https://doi.org/10.1080/13588265.2020.1838158>
- [30] European Aviation Safety Agency, "Normal, Utility, Aerobatic and Commuter Aeroplanes," Certification Specifications, Part 23, Occupant Physical Environment.
- [31] Hedayati, R., and Sadighi, M., "Effect of Using an Inner Plate Between Two Faces of a Sandwich Structure in Resistance to Bird-Strike Impact," *Journal of Aerospace Engineering*, Vol. 29, No. 1, 2016, Paper 04015020.
[https://doi.org/10.1061/\(ASCE\)AS.1943-5525.0000505](https://doi.org/10.1061/(ASCE)AS.1943-5525.0000505)
- [32] Federal Aviation Administration, Federal Aviation Regulations, Part 25, Bird Strike Damage.
- [33] Abdi, F., Talagani, M. R., Godines, C., and Montero, M. V., "Impact and Post Impact Delamination Evolution of Honeycomb Sandwich Structure," *NAFEMS World Congress Conference Proceedings*, June 2015.
- [34] Heimbs, S., Middendorf, P., and Maier, M., "Honeycomb Sandwich Material Modeling for Dynamic Simulations of Aircraft Interior Components," *9th International LS-DYNA Users Conference*, Vol. 20, June 2006, pp. 1–13.
- [35] Sadighi, M., Dehkordi, A. A., and Khodambashi, R., "A Theoretical and Experimental Study of Failure Maps of Sandwich Beams with Composite Skins and Honeycomb Core," *AUT Journal of Modeling and Simulation*, Vol. 42, No. 1, 2010, pp. 37–47.
- [36] Yu, Z., Xue, P., Yao, P., and Zahran, M. S., "Novel Design of Wing Leading Edge Against Birdstrike," *Journal of Aerospace Engineering*, Vol. 33, No. 3, 2020, Paper 04020009.
[https://doi.org/10.1061/\(ASCE\)AS.1943-5525.0001120](https://doi.org/10.1061/(ASCE)AS.1943-5525.0001120)
- [37] Kumar, Y. B., "Design and Analysis of a New Type of Aircraft Wing Leading Edge Against Bird-Impact," *Research Journal of Engineering*, Vol. 6, No. 3, 2017, pp. 23–47.
- [38] Kılıçaslan, C., Odacı, İ. K., Taşdemirci, A., and Güden, M., "Experimental Testing and Full and Homogenized Numerical Models of the Low Velocity and Dynamic Deformation of the Trapezoidal Aluminium Corrugated Core Sandwich," *Strain*, Vol. 50, No. 3, 2014, pp. 236–249.
<https://doi.org/10.1111/str.12085>